MNRAS **000**, 000–000 (0000) Preprint 3 January 2020 Compiled using MNRAS LATEX style file v3.0

AGN feedback in the FR II galaxy 3C 220.1

Wenhao Liu[1⋆], Ming Sun[1]†, Paul E. J. Nulsen[2,3], Diana M. Worrall[4], Mark Birkinshaw[4], Craig Sarazin[5], William R. Forman[2], Christine Jones[2], Chong Ge[1]

[1] *Department of Physics and Astronomy, University of Alabama in Huntsville, Huntsville, AL 35899, USA*
[2] *Harvard-Smithsonian Center for Astrophysics, 60 Garden Street, Cambridge, MA 02138, USA*
[3] *ICRAR, University of Western Australia, 35 Stirling Hwy, Crawley, WA 6009, Australia*
[4] *HH Wills Physics Laboratory, University of Bristol, Tyndall Avenue, Bristol BS8 1TL, UK*
[5] *Department of Astronomy, University of Virginia, Charlottesville, VA 22904, USA*

3 January 2020

ABSTRACT

We present results from a deep (174 ks) *Chandra* observation of the FR-II radio galaxy 3C 220.1, the central brightest cluster galaxy (BCG) of a $kT \sim 4$ keV cluster at $z = 0.61$. The temperature of the hot cluster medium drops from ~ 5.9 keV to ~ 3.9 keV at ~ 35 kpc radius, while the temperature at smaller radii may be substantially lower. The central active galactic nucleus (AGN) outshines the whole cluster in X-rays, with a bolometric luminosity of 2.0×10^{46} erg s^{-1} ($\sim 10\%$ of the Eddington rate). The system shows a pair of potential X-ray cavities ~ 35 kpc east and west of the nucleus. The cavity power is estimated within the range of 1.0×10^{44} erg s^{-1} and 1.7×10^{45} erg s^{-1}, from different methods. The X-ray enhancements in the radio lobes could be due to inverse Compton emission, with a total 2-10 keV luminosity of $\sim 8.0 \times 10^{42}$ erg s^{-1}. We compare 3C 220.1 with other cluster BCGs, including Cygnus A, as there are few BCGs in rich clusters hosting an FR-II galaxy. We also summarize the jet power of FR-II galaxies from different methods. The comparison suggests that the cavity power of FR-II galaxies likely under-estimates the jet power. The properties of 3C 220.1 suggest that it is at the transition stage from quasar-mode feedback to radio-mode feedback.

Key words: galaxies: groups: individual: 3C 220.1 – X-rays: galaxies: clusters – galaxies: jets

1 INTRODUCTION

It has been widely accepted that feedback from central active galactic nuclei (AGN) plays an important role in galaxy formation and evolution (e.g., McNamara & Nulsen 2007; Fabian 2012). In the nearby Universe, a strong central AGN, hosted by the brightest cluster galaxy (BCG) in the core of the galaxy cluster, can drive energetic radio jets, which propagate through the intracluster medium (ICM), push aside the hot X-ray gas, and create cavities visible in X-ray images (e.g., Churazov et al. 2001). At low redshift, the X-ray cavities are predominantly found in cool-core clusters, with a high detection rate of 90% (e.g., Dunn & Fabian 2006; Fabian 2012), although cases in non-cool core clusters have also been reported (e.g., Worrall & Birkinshaw 2017). This is known as "radio-mode" AGN feedback, which is mainly mechanically dominated and occurs when the central black holes (BHs) are accreting at a low rate compared to the Eddington limit. The radio AGN affects the ICM through AGN-driven shocks and bubbles. The high mechanical power of radio AGN can not only quench cooling in cluster cool cores, but can also drive the ICM properties away from those defined by simple self-similar relations involving only gravity (e.g., Voit 2005). The features in the ICM, such as cavities and shocks discovered by high-resolution X-ray observations, can serve as calorimeters for the total energy output of the central AGN, allowing important constraints on the evolution of the central super-massive black hole (SMBH) (e.g., McNamara & Nulsen 2007; Fabian 2012).

Large cavities in the ICM and the associated AGN shocks trace the biggest explosions in the Universe. A correlation between the AGN radio luminosity and jet power, or the $L_{radio} - P_{jet}$ relation, has been established (Bîrzan et al. 2008; Cavagnolo et al. 2010; O'Sullivan et al. 2011). Thus, a natural approach to study the biggest AGN explosions is to

⋆ E-mail: wl0014@uah.edu
† E-mail: ms0071@uah.edu

study the most powerful FR II galaxies. However, very few powerful FR II galaxies have been included in the studies of X-ray cavities. In the combined samples from the literature (e.g., Bîrzan et al. 2008; Cavagnolo et al. 2010; O'Sullivan et al. 2011; Hlavacek-Larrondo et al. 2012), Cygnus A and 3C 295 are the only two FR II galaxies. Besides these, the powerful FR II radio galaxies, 3C 444 (Croston et al. 2011; Vagshette et al. 2017), and 3C 320 (Vagshette et al. 2019), have been studied in detail for X-ray cavities.

At high redshift ($z > 1$), AGN feedback is mainly radiatively dominated, in the so-called "quasar-mode", which occurs when the central BHs are accreting at rates near the Eddington limit. Using a sample of $z > 0.3$ BCGs, Hlavacek-Larrondo et al. (2012, 2013) found that the X-ray AGN luminosities in BCGs increase with redshift, while the mechanical properties of the AGN outflows remain unchanged. The central AGN in such systems provide both strong radiative and mechanical feedback, suggesting that they are in the process of transitioning between quasar-mode feedback and radio-mode feedback (e.g., O'Sullivan et al. 2012; Hlavacek-Larrondo et al. 2015). The detection rate of cavities in BCGs at higher redshift is relatively small, e.g., $\sim 25\%$ in a sample of 76 clusters in Massive Cluster Survey within $0.3 < z < 0.7$ (Hlavacek-Larrondo et al. 2012) and $\sim 7\%$ in a sample of 86 SPT-selected clusters within $0.4 < z < 1.2$ (Hlavacek-Larrondo et al. 2015), as in general, long *Chandra* observations are required to detect the cavities in X-rays at high redshift. The systems showing both radiative feedback and radio-mode feedback with detailed X-ray studies are very few. These include H1821+643 ($z = 0.299$) (Russell et al. 2010), IRAS 09104+4109 ($z = 0.442$) (O'Sullivan et al. 2012), and the Phoenix cluster ($z = 0.596$) (McDonald et al. 2015). It is crucial to build a census of AGN feedback in such high redshift systems to understand how and why the SMBHs switch from one mode to the other.

3C 220.1 is classified as an FR II narrow emission line radio galaxy at redshift $z = 0.61$ (Spinrad et al. 1985), with two prominent radio lobes that extend over 100 kpc from the nucleus. In Fig. 1 we show the VLA images of 3C 220.1 at 1.5, 4.9 GHz from program AA267, and 8.4 GHz from program AP380 (e.g., Worrall et al. 2001; Mullin et al. 2006; Fernini 2014). The radio source has a core, one-sided deflected radio jet to the east and three "hotspot-like" structures as shown in Fig. 1 bottom right. 3C 220.1 was observed with the *ROSAT* HRI, which allowed the emission to be decomposed into a compact core and an extended component (e.g., Hardcastle et al. 1998; Worrall et al. 2001; Belsole et al. 2007). A subsequent short ($\sim$ 18 ks) *Chandra* observation confirmed two components, and showed that 3C 220.1 is the BCG of a massive cluster with a temperature of $\sim$ 5 keV (Worrall et al. 2001). Although optical observations show no evidence of a rich cluster near 3C 220.1, the galaxy cluster containing 3C 220.1 hosts a giant luminous arc, which is $\sim 9''$ away from the center and subtends $\sim 70^\circ$ around the radio galaxy, as observed with the *Hubble Space Telescope* (*HST*) in Fig. 2. The cluster is indeed massive for its redshift, with a virial mass of $3.5 \times 10^{14}\ M_\odot$ estimated from strong lensing (Comerford & Natarajan 2007). The cluster hosts a large X-ray cool core, with a central cooling time less than 1 Gyr (Worrall et al. 2001). The BCG is still actively forming stars, with *HST* data suggesting a star formation rate of $\sim 21 - 67\ M_\odot\ \mathrm{yr}^{-1}$ (Westhues et al. 2016). We summarize the cluster properties of 3C 220.1 in Table 1. The central X-ray AGN is very luminous with a 0.7-12 keV luminosity of $\sim 10^{45}$ erg s^{-1} (Worrall et al. 2001), suggesting that 3C 220.1 is undergoing strong radiative feedback. Here, we present a detailed study with deep (170 ks) *Chandra* observations to explore the AGN feedback in 3C 220.1.

In this paper we adopt a cosmology with $H_0 = 70$ km s^{-1} Mpc^{-1}, $\Omega_\mathrm{M} = 0.3$, and $\Omega_\Lambda = 0.7$. At a redshift of $z = 0.61$, the luminosity distance is 3601.4 Mpc and $1''$ corresponds to 6.736 kpc. All error bars are quoted at 1σ confidence level, unless otherwise specified.

2 CHANDRA DATA ANALYSIS

3C 220.1 was observed with *Chandra* for $\sim$ 170 ks split into four observations (Obs. IDs 17130, 17131, 18747, and 18860, PI: Sun) in January and June 2016 with the Advanced CCD Imaging Spectrometer (ACIS). All four observations placed the core on chip S3 and were taken in Very Faint (VFAINT) mode. The details of the *Chandra* observations are summarized in Table 2. There also was one $\sim$ 19 ks ACIS-S observation in 1999, published by Worrall et al. (2001). In this study we focus on the new, deep data in 2016, due to significant changes in the characteristics of the instrument between these dates. The data were analyzed using CIAO 4.9 and CALDB version 4.7.4 from the *Chandra* X-ray Center. For each observation the level 1 event files were reprocessed using the `CHANDRA_REPRO` script to account for afterglows, bad pixels, charge transfer inefficiency, and time-dependent gain correction. The improved background filtering was also applied by setting `CHECK_VF_PHA` as "yes" to remove bad events that are likely associated with cosmic rays. The background light curve extracted from a source-free region was filtered with the `LC_CLEAN` script[1] to identify any period affected by background flares. There were no strong background flares for these observations and the resulting cleaned exposure time is given in Table 2.

In order to correct for small astrometric errors, we chose ObsID 18747 as the reference due to its longest exposure. For each observation, a broad band (0.5-7.0 keV energy band) image on the S3 chip was made and point sources were detected. The astrometric translation required to align each data set with the reference data was obtained using the CIAO tool `wcs_match`, and was applied to each event list using the CIAO tool `wcs_update`.

Point sources were detected in the combined 0.5-7.0 keV count image using the CIAO tool `WAVDETECT`, with the variation of the point spread function across the field considered. The detection threshold was set to 10^{-6} and the scales are from 1 to 16 pixels, increasing in steps of a factor of $\sqrt{2}$. All detected sources were visually inspected and masked in the analysis except the central AGN. A weighted exposure map was generated to account for quantum efficiency, vignetting and the energy dependence of the effective area assuming an absorbed APEC model with $kT = 4.0$ keV, $N_\mathrm{H} = 2.0 \times 10^{20}$ cm^{-2} (the weighted column density of the total Galactic hydrogen absorption, calculated by the "NHtot" tool[2]), and

[1] http://asc.harvard.edu/contrib/maxim/acisbg/
[2] http://www.swift.ac.uk/analysis/nhtot/index.php

Table 1. Properties of the 3C 220.1 cluster

Name	z	$kT_{500}{}^{a}$ (keV)	Z^{a}	$L_{X,500}{}^{a}$ (10^{44} erg s^{-1})	$M_{500}{}^{a}$ (10^{14} M$_{\odot}$)	$P_{1.4GHz}$ (10^{27} W Hz^{-1})	radio spectral index^{b}
3C 220.1	0.61	$3.7^{+0.9}_{-0.6}$	$0.5^{+0.6}_{-0.4}$	2.5 ± 0.4	$1.3^{+0.6}_{-0.3}$	3.4 ± 0.1	-0.97 ± 0.02

a: Temperature and abundance are measured within $0.15 - 0.75R_{500}$ ($\sim 16'' - 80''$). The X-ray bolometric luminosity is measured within R_{500} based on the surface brightness profile. The gravitational mass is estimated based on the $M - T$ relation (Sun et al. 2009). Based on the established $L - T$ relation, the estimated luminosity from the hot ICM, after correcting for the cosmological evolution term $E(z)$, is $\sim 2.0 \times 10^{44}$ erg s^{-1} from Giles et al. (2016), or $\sim 4.2 \times 10^{44}$ erg s^{-1} from Sun (2012). *b*: The fitted radio spectral index across the whole source from 38 MHz to 10 GHz based on the data from NED.

Table 2. *Chandra* Observations of 3C 220.1 (PI: Sun)

ObsID	Date Obs	Total Exp (ks)	Cleaned Exp (ks)
17130	2016 Jan 17	41.51	40.94
17131	2016 Jun 02	49.40	49.13
18747	2016 Jan 25	54.34	54.25
18860	2016 Jun 05	28.65	28.65

abundance of 0.3 $Z_{\odot}$ at the redshift $z = 0.61$. We used the CALDB blank sky background files in our data analysis. For each observation the standard blank sky file for each chip was reprojected to match the time dependent aspect solution, and normalized to match the count rate in the 9.5-12.0 keV band to account for variations in the particle background. We estimated the local X-ray background for 3C 220.1 in each observation using a region where the surface brightness is approximately constant. The regions are $> 3.0'$ from the cluster on the S3 chip. For spectral fitting, we used XSPEC version 12.10.0 and AtomDB 3.0.9, assuming the solar abundance table by Asplund et al. (2009). The absorption model is `TBABS`.

3 SPATIAL AND SPECTRAL ANALYSIS

3.1 Spatial Analysis

We reprojected and summed the count images, background images, and exposure maps respectively from four observations using the CIAO tool `reproject_image`. Fig. 3 left panel shows the combined background-subtracted, exposure-corrected image in the 0.5-3.0 keV band, smoothed with a two dimensional Gaussian 2-pixel kernel ($0''.492$/pixel) and overlaid with the VLA 1.5 GHz and 8.4 GHz radio contours. Fig. 3 right panel shows the same X-ray image, but with the central bright AGN masked, smoothed with a Gaussian 3-pixel kernel. X-ray enhancements, associated with the radio lobes, are visible in the figure.

Azimuthal surface brightness values were examined to determine the significance of potential cavities. As shown in Fig. 4 (left panel), we extracted the surface brightness profiles in two annular regions centered on the nucleus with inner and outer radii of $3''$-$8''$ and $8''$-$20''$ to investigate the azimuthal variations. Fig. 4 right shows the azimuthal variations of the surface brightness with an angle step size of 20° in the inner and outer regions in the 0.5-2.0 keV band. The inner surface brightness profiles show depressions around 10°-30° and 150°-210° (measured counterclockwise from the west), because of the potential cavities, while the surface brightness profile in the outer region (corresponding to the radio lobes) shows enhanced emission. This may be due to inverse Compton X-ray emission (see Section 4.6), which is often found in FR II radio lobes, and which was reported for 3C 220.1 based on the earlier *Chandra* data by Croston et al. (2005).

3.2 Cluster Surface Brightness Profile

In order to study the arcsecond-features of the central bright source, we created subpixel ($0.0984''$/pixel) images by using the Energy-Dependent Subpixel Event Repositioning (EDSER) algorithm (Li et al. 2004). The radial surface brightness profiles obtained from the subpixel images in the soft and hard X-ray bands for 3C 220.1 are shown in Fig. 5. The central point source is bright and dominates the central region. To derive the gas properties for the cluster, we simulated the PSF of the central point source using the *Chandra* Ray Tracer (ChaRT) program (Carter et al. 2003). We first fitted the central AGN spectrum with a power-law model (see section 4.1) and used the best-fitting model as the input for the ChaRT program. The simulation was then projected onto the ACIS-S detector with the MARX (version 5.3.2) software[3] and used to estimate the PSF contamination from the total emission. The parameter `AspectBlur` of MARX is used to account for the known uncertainty in the determination of the aspect solution. The parameter can be adjusted to better match the PSF core and wing to observations. In our study we used the default `AspectBlur` value of $0''.25$ for ACIS-S observations. Fig. 5 shows the simulated PSF (blue) and the total observed surface brightness profile (black) in soft (0.5-2.0 keV) and hard (2.0-7.0 keV) bands. The PSF was normalized based on the total counts in the central $2''$.

3.3 Spectral Analysis

Spectra were extracted from the same circular annuli for the four observations separately using the CIAO tool `specextract`. For each spectrum, the weighted response files and matrices were made, and a corresponding background spectrum was extracted from the same region from the blank sky background data. The spectra were fitted in the energy band 0.5-5.0 keV using the C-statistic (Cash 1979), since it is largely unbiased compared to χ^2 minimization (e.g., Humphrey et al. 2009). The spectra from the same region

[3] https://space.mit.edu/CXC/MARX/

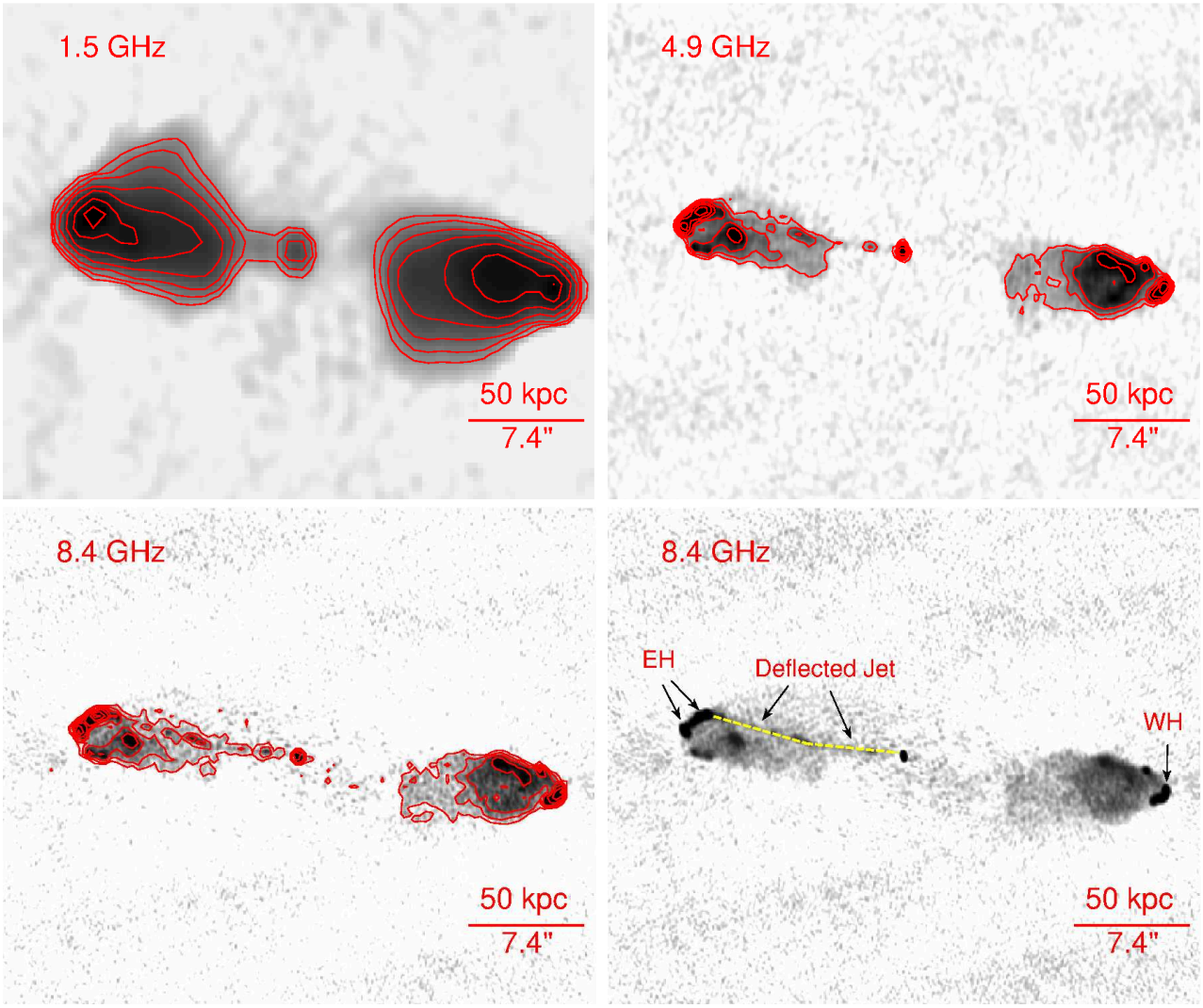

Figure 1. VLA images and contours of 3C 220.1 at 1.5 GHz (top left), 4.9 GHz (top right), and 8.4 GHz (bottom left) with resolution of 1.8 × 1.4 arcsec, 0.5 × 0.3 arcsec, and 0.3 × 0.2 arcsec. The contours start at 2σ and are spaced by a factor of 2 in intensity. The 8.4 GHz radio image (bottom right) shows three "hotspot-like" structures (two eastern hotspots, EH, and one western hotspot, WH) and a deflected jet (with a deflection angle of $\sim 14°$) on the eastern side (highlighted with dashed yellow curve). The projected distances of the farthest points of the radio lobes to the nucleus are ~ 97 and ~ 120 kpc for the east and west, respectively.

from four observations were fitted simultaneously to an absorbed thermal APEC model, i.e., `TBABS*APEC`. The temperature, metallicity, and the normalization were allowed to vary freely. For regions where the abundances cannot be well constrained due to the few source counts, we fixed the abundance at the value obtained in nearby regions.

We focused our analysis on the ACIS-S3 chip and extracted a set of 5 circular annuli from the center to a radius of ~ 540 kpc. For the temperature deprojection, we adopted a model-independent approach (Sun et al. 2003; Liu et al. 2019) which can account for point sources and chip gaps. The deprojected temperature profile is shown in Fig. 6 (top left). We excluded the central ~ 20 kpc radius ($\sim 3''$) due to the central bright point source. The deprojected temperature decreases towards the center, from ~ 5.9 keV at 215 kpc to ~ 3.9 keV at 37 kpc, although the uncertainties are too large to make the drop significant. On the other hand, as shown in Section 4.1, the gas temperature within the central 20 kpc radius can be substantially lower. The electron density (Fig. 6 bottom left) was obtained directly from the deprojected normalization of the APEC component, assuming $n_e = 1.22 n_H$, where n_e and n_H are the electron and proton densities. Based on the deprojected gas temperature and density, we calculated the pressure (Fig. 6 top right) in each annulus as $P = nkT$ (where $n = 1.92 n_e$) and the entropy (Fig. 6 middle right) as $S = kT/n_e^{-2/3}$. The cooling time (shown in Fig. 6 bottom right) is defined as $t_{cool} = 3P/[2 n_e n_H \Lambda(T, Z)]$, where $\Lambda(T, Z)$ is the cooling function determined by the gas temperature and metallicity. Assuming that the cluster was born at a redshift of 2.0, we estimated a cluster age of ~ 4.5 Gyr. This gives a cooling radius of 71 kpc, if we define it as the radius where the cooling time equals the cluster age. We derive a bolometric luminosity of 1.5×10^{44} erg s^{-1} within the cooling radius.

Assuming hydrostatic equilibrium and spherical sym-

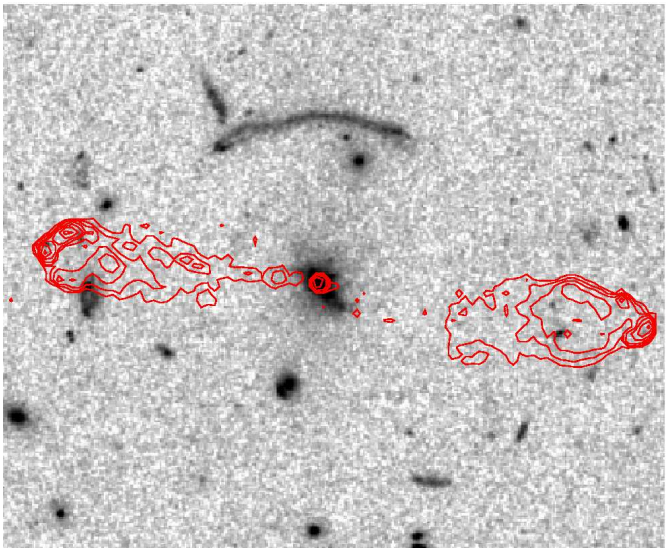

Figure 2. The *HST* WFPC2 F555W image of 3C 220.1 (roughly corresponding to the rest-frame U band), from the *HST* program ID 6778, overlaid with the VLA 8.4 GHz radio contours (in red) as in Fig. 1. This shows the irregular morphology of the BCG that may imply star formation and a large strong-lensing arc to the north.

metry, we calculate the gravitational acceleration, g, as

$$g = \frac{d\Phi}{dr} = -\frac{1}{\rho}\frac{dP}{dr}, \quad (1)$$

where Φ is the gravitational potential, $\rho = 1.92 n_{\rm e} \mu m_{\rm p}$ is the particle gas density, $\mu = 0.60$ is the mean particle weight and $m_{\rm p}$ is the proton mass. To obtain a smooth pressure profile, we fitted it with a generalized NFW model, where $P \propto r^{-3}$ at large radii and the inner slope is allowed to vary. We found the best-fitting inner slope of 0.58 ± 0.11. Once the gravitational acceleration is determined, we calculated the free fall time $t_{\rm ff} = \sqrt{\frac{2r}{g}}$ (e.g., Gaspari et al. 2012). As shown in Fig. 7, the minimum value of $t_{\rm cool}/t_{\rm ff}$ is ~ 30, where the cooling time is ~ 1.7 Gyr. Although this value is larger than the typical threshold ($\sim 10 - 20$) for precipitation (Sharma et al. 2012; Gaspari et al. 2012; Voit et al. 2015), it is possible that the threshold can be reached within the central ~ 20 kpc.

We estimated the total gravitational mass assuming hydrostatic equilibrium for the hot gas in the gravitational potential. We already calculated the gravitational acceleration g, and the total gravitational mass is therefore, $M(r) = g(r)r^2/G$, where G is the gravitational constant. The total gravitational mass profile is shown in Fig. 8. The hydrostatic mass estimate is consistent with the previous mass estimate using strong lensing (e.g., Comerford & Natarajan 2007).

We measured X-ray temperature, kT_{500}, within $0.15 - 0.75R_{500}$ ($\sim 16'' - 80''$). Using the surface brightness profile, after removing the PSF of the central AGN, we calculated the flux from the hot ICM in the central region (e.g., within $0.15R_{500}$) and outer region ($> 0.75R_{500}$), and estimate a bolometric luminosity within R_{500}, $L_{X,500}$, of $2.5 \pm 0.4 \times 10^{44}$ erg s^{-1}. Based on the established $L - T$ relation, the estimated luminosity based on the fitted temperature, after correcting for the cosmological evolution term $E(z)$, is $\sim 2.0 \times 10^{44}$ erg s^{-1} from Giles et al. (2016), or $\sim 4.2 \times 10^{44}$ erg s^{-1} from Sun (2012).

4 DISCUSSION

4.1 The Central AGN

To study the central AGN, we reprocessed the *Chandra* data by setting `CHECK_VF_PHA` as "no", since it could remove good events in observations with bright point sources by setting to "yes". We extracted spectra of the central X-ray source from each observation in a circular region with a radius of $2''$, and the background spectra from an annulus from $2''$ to $4''$. The total net counts from four observations are ~ 8000 over the 0.5-7.0 keV energy band. The spectra from the four observations were fitted simultaneously between 0.5 and 7.0 keV. The power-law photon index is 1.62 ± 0.02 from a single power-law model (Table 3), close to the canonical AGN value of 1.7. We attempted a model with an obscured AGN plus a soft component, which indeed improves the spectral fits (Table 3). 3C 220.1's AGN is obscured with a small intrinsic absorption column density of $\sim 0.3 \times 10^{22}$ cm^{-2}. The rest-frame 2-10 keV luminosity of the AGN is $\sim 5.0 \times 10^{44}$ erg s^{-1}. We found that the luminosity of the AGN is increased by $\sim 5\%$ by setting `CHECK_VF_PHA` to "no". Using a bolometric correction of 40 from Vasudevan & Fabian (2007), we estimate the bolometric luminosity of the central AGN to be $\sim 2.0 \times 10^{46}$ erg s^{-1}. We considered the aperture correction factor for the central AGN luminosity, since the aperture ($2''$-$4''$) used as background still contains emission from the central AGN. However, based on the simulated PSF of the central point source, we found that the aperture correction factor is very small ($< 1\%$). We checked the pileup fraction by using the model jdpileup (Davis 2001) and found that the pileup fraction is $< 2\%$.

We examined the 2-10 keV variability of the central point source. As shown in Table 2, the time span of the four observations is about half a year. Since AGN variabilities have different timescales, we also include the previous, short ACIS-S observation (Obs. ID 839) taken in 1999. We found the 2-10 keV flux changes by $\sim 7\%$ during the four recent observations, and the flux from new observations is $\sim 30\%$ higher than that from the old observation, based on our own AGN spectrum fitting from the old observation, and the previous study (Belsole et al. 2006). In the new data, we also checked the possible X-ray emission associated with the radio features, e.g., radio jet and the hot spots. We chose a circular region for the hot spots and a box region for the radio jet to measure the observed X-ray emission as in Massaro et al. (2015). Background regions of the same shape and size, were chosen to avoid emission from other sources, with two boxes for the radio jet, and three circles for the hot spots. There is marginal X-ray emission detected from the eastern radio hotspots with a significance of $\sim 1.6\ \sigma$, and there is no X-ray emission detected from the western hotspot or from the radio jet. Assuming an absorbed power-law model with a photon index of 2.5, we estimated a 0.5-10 keV luminosity of $\sim 3.7 \times 10^{41}$ and $\sim 2.7 \times 10^{41}$ erg s^{-1} for two eastern radio hot spots.

Based on the 5 GHz radio-core flux density (25 mJy; Giovannini et al. 1988), we calculated a radio luminosity at

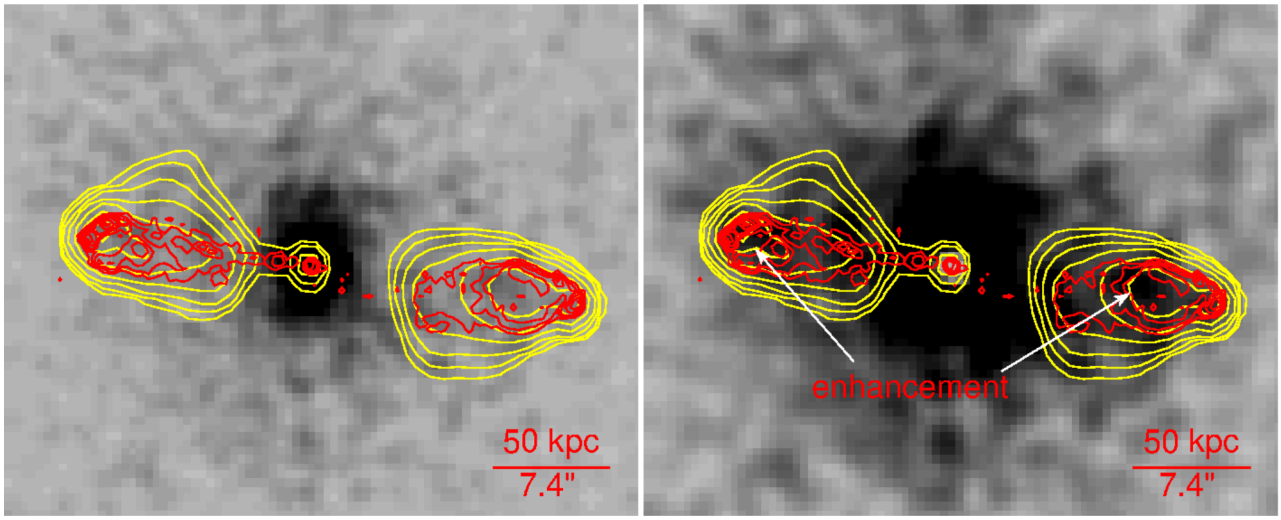

Figure 3. *Left*: The combined background-subtracted, exposure-corrected *Chandra* image of 3C 220.1 in the 0.5-3.0 keV band, smoothed with a two dimensional Gaussian 2-pixel kernel (0.492″/pixel) and overlaid with the VLA 1.5 GHz (yellow) and 8.4 GHz (red) radio contours. *Right*: The same *Chandra* image as in the left panel, smoothed with a 2D Gaussian 3-pixel kernel (0.492″/pixel). We have masked the central bright AGN (2″ radius to cover much of the PSF). X-ray enhancements are visible in eastern and western radio lobe regions.

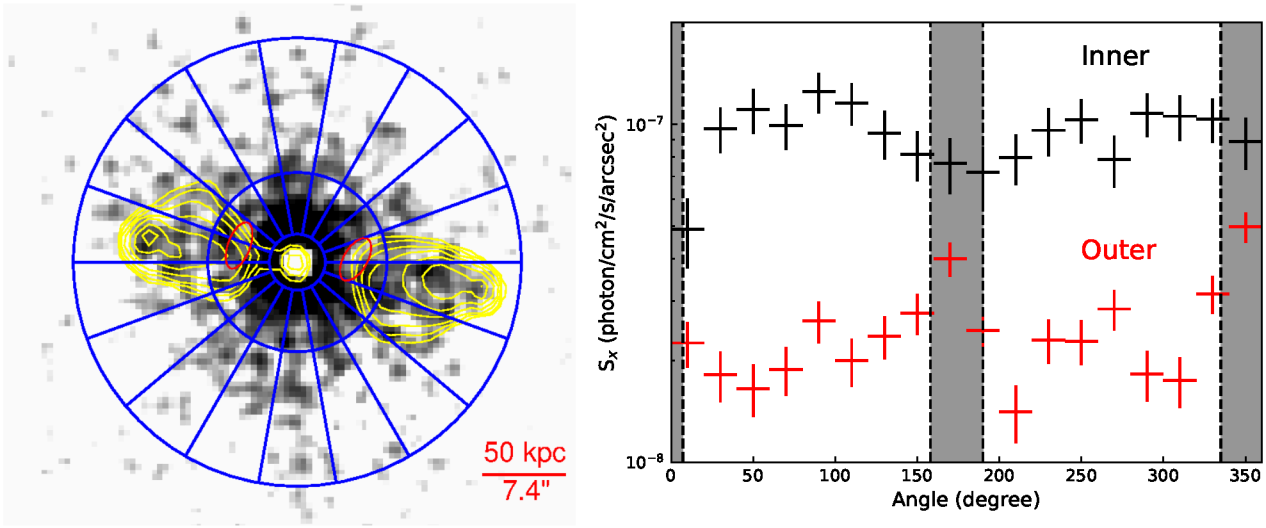

Figure 4. Left: Exposure-corrected, background-subtracted *Chandra* image (0.5-2.0 keV) of 3C 220.1, smoothed with a Gaussian 2-pixel kernel, overlaid with VLA 1.5 GHz contours. The overlaid blue regions denote two annuli (3″-8″and 8″-20″) where the azimuthal surface brightness profiles are extracted. The red ellipses denote the potential cavities showing surface brightness depressions as in the right panel. Right: The surface brightness profiles extracted along the azimuthal directions (measured counterclockwise from the west) with angle step size of 20 degrees from inner 3″-8″annulus (black) and outer 8″-20″annulus (red) in 0.5-2.0 keV band. The grey region between the dashed lines shows the range for the eastern ($158^\circ - 190^\circ$) and western ($-25^\circ - 7^\circ$) radio lobes. The inner surface brightness profile shows depressions around $-10^\circ - 30^\circ$ and $150^\circ - 210^\circ$. The outer surface brightness profile shows enhanced emission in the region corresponding with the eastern and western radio lobes.

5 GHz of $L_{\rm R} \approx 2 \times 10^{42}$ erg s^{-1} assuming the spectra index of -0.6. Using the black hole fundamental plane (Gültekin et al. 2009), i.e., the relation between the radio luminosity at 5 GHz, the X-ray 2-10 keV luminosity, and the black hole mass, we estimate a black hole mass of $\sim 1.3 \times 10^9$ $M_\odot$. Assuming a radiative efficiency $\epsilon = 0.1$, we estimate an Eddington luminosity $L_{\rm Edd}$ of 1.6×10^{47} erg s^{-1}, giving an Eddington ratio $L_{\rm bol}/L_{\rm Edd}$ of ~ 0.13.

4.2 Cavity Power

In Fig. 4 (left panel), the potential cavities, defined by the surface brightness depressions, are close to the central nucleus and are smaller than the radio lobes. This is similar to some other high-redshift cool core systems, where the cavities are generally found in the central gas-rich regions (e.g., Hlavacek-Larrondo et al. 2015). This may suggest that cavi-

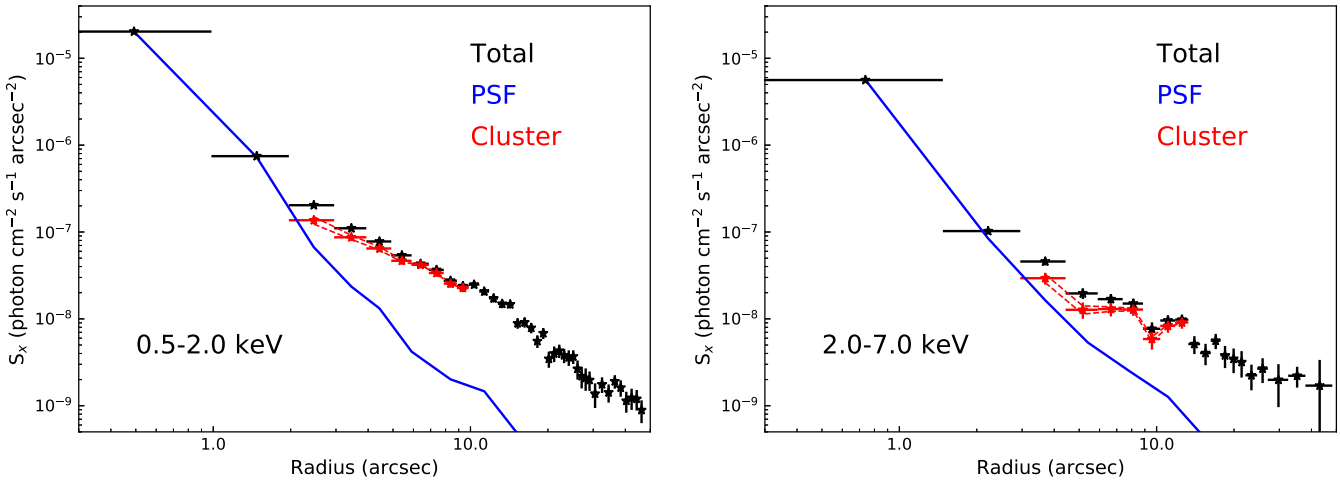

Figure 5. Left: Total surface brightness profile in the energy range of 0.5-2.0 keV for 3C 220.1 (black), the simulated PSF (blue) of the central point source using ChaRT simulation, and the cluster surface brightness profile produced by subtracting the simulated PSF from the total surface brightness (red). We normalized the PSF assuming that the central 2″ is dominated by the AGN. The red dashed lines show the change on the cluster emission when the AGN normalization is changed by 20%. Right: Same as left, but in the 2.0-7.0 keV band. We do not plot the cluster surface brightness profile (red) to large radii since it would overlap with the total surface brightness profile in black.

Table 3. Spectral fits of the central AGN

Model	$\Gamma_1{}^a$	kT^b (keV)	$N_{\rm H,intr}{}^c$ (10^{22} cm^{-2})	$L_{0.5-2.0}{}^d$ (10^{43}erg s^{-1})	$L_{2-10}{}^e$ (10^{44}erg s^{-1})	$[C,C_e,C_\sigma]^f$
tbabs*POW	$1.62^{+0.02}_{-0.02}$				$5.17^{+0.07}_{-0.07}$	[166.9, 148.6, 17.3]
tbabs*(ztbabs*POW+APEC)	$1.64^{+0.08}_{-0.08}$	$1.05^{+0.20}_{-0.14}$	$0.28^{+0.15}_{-0.08}$	$3.77^{+0.82}_{-0.78}$	$5.16^{+0.08}_{-0.08}$	[148.0, 148.6, 17.3]

a: the photon index for the power-law component; b: the temperature for the thermal component (we assumed an abundance of 0.5 $Z_\odot$. The fits are not sensitive to the assumed abundance value.); c: the column density for the intrinsic absorption; d: the rest-frame 0.5-2.0 keV luminosity for the thermal component; e: the rest-frame 2-10 keV luminosity for the power-law component; f: C, C_e, C_σ are the fitted C-statistic, its expected value, and its standard deviation computed based on Kaastra (2017). 68% of the time the acceptable spectral models should have $-1 < \frac{C-C_e}{C_\sigma} < 1$.

ties are created recently and have not buoyantly risen to the large radii. On the other hand, the actual cavities may be larger, since they could be obscured by the bright AGN at small radii and the enhanced X-ray emission from the lobes (discussed in Section 4.6) and projection at large radii.

We estimated a lower limit for the total jet power based on the enthalpy and buoyant rise time of the cavities (Churazov et al. 2001), to allow a direct comparison with previous studies. We assumed the eastern and western cavities are ellipsoids as in Fig. 4. The projected distances of the eastern and western cavity centers to the nucleus are ~ 36.4 kpc and ~ 35.0 kpc. The major and minor axes are 14.6 kpc and 6.7 kpc for the eastern cavity, and 14.2 kpc and 7.2 kpc for the western cavity. The path length along the line of sight, calculated as the square root of the product of major and minor axes, are 9.9 kpc and 10.1 kpc, respectively. The estimated rise times of the bubbles to their present position are 8.8×10^7 yr and 8.3×10^7 yr. The total enthalpy ($H = 4PV$, where P is the azimuthally-averaged pressure at the radius of the center of the cavity) is calculated from the projected temperature and electron density profile. The total enthalpy and the cavity power for the two cavities are 2.7×10^{59} erg and $\sim 1.0\times10^{44}$ erg s^{-1}. We note that the cavity power is slightly smaller than the cooling luminosity (section 3.3). Since the cavities here could be under-estimated, we also estimate the jet power assuming the cavities are as large as the radio lobes. With a projected distance of ~ 65 kpc to the nucleus, and major and minor axes of 40 and 20 kpc for both radio lobes, the total enthalpy and power for two cavities are $\sim 3\times10^{60}$ erg and $\sim 1.7\times10^{45}$ erg/s. We consider the actual cavity power in 3C 220.1 lies probably between these two estimates.

If the cavity center does not lie on the plane of sky, we need to consider projection effect on the estimated cavity power. Since the actual distance from the AGN to the center of cavity and the size of cavity would increase, the pressure at the center of cavity would be lower, while the volume of cavity would increase, hence affecting the estimated total enthalpy. In addition, the estimated age of the cavity will increase. Based on the jet to counter-jet ratio, Worrall et al. (2001) measured a maximum angle of ~ 67 degree of the jet to the line of sight for 3C 220.1, which can be assumed as

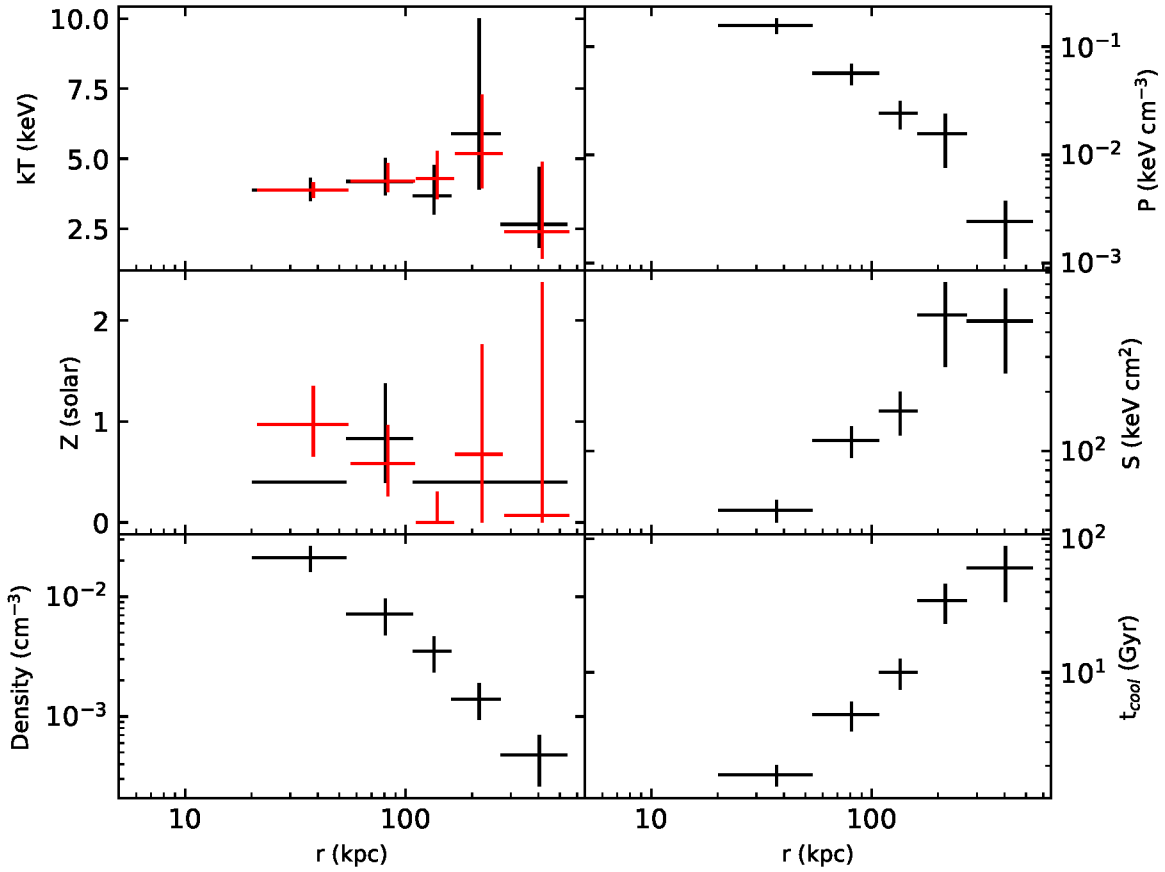

Figure 6. Radial profiles of the deprojected temperature, abundance, electron density, pressure, entropy, and cooling time. We also show the projected temperature and abundance profiles in red (we slightly shifted the red points horizontally for comparison). We fix the deprojected abundance in all radial bins except the second bin.

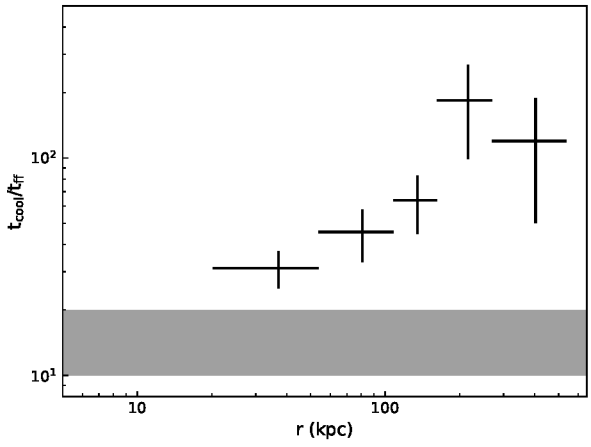

Figure 7. Radial profile of $t_{\rm cool}/t_{\rm ff}$. The grey region shows the typical threshold for precipitation, $\min(t_{\rm cool}/t_{\rm ff})\approx 10-20$, below which the hot gas becomes thermally unstable (Sharma et al. 2012; Gaspari et al. 2012; Voit et al. 2015).

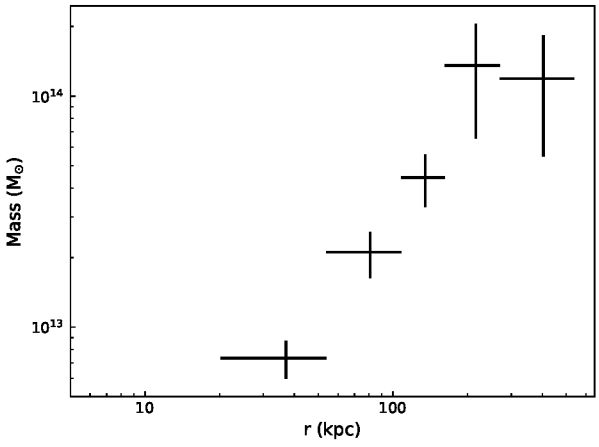

Figure 8. The total gravitational mass profile for the cluster 3C 220.1 derived assuming hydrostatic equilibrium and spherical symmetry.

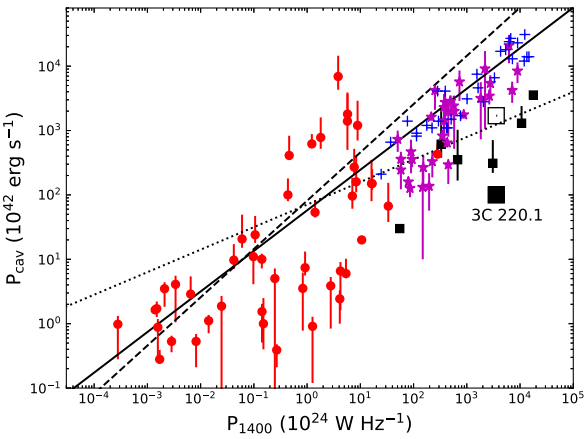

Figure 9. Cavity power versus radio power at 1.4 GHz for galaxy groups and clusters. Red circles denote FR-I sources from Bîrzan et al. (2008), Cavagnolo et al. (2010), and O'Sullivan et al. (2011), with their best-fitting relations in dotted, dashed, and solid lines, respectively. For systems in common between these papers we used the values from O'Sullivan et al. (2011). Black squares denote FR-II sources, i.e., Cygnus A (Rafferty et al. 2006), Hercules A (Rafferty et al. 2006), PKS B2152-699 (Worrall et al. 2012), 3C 295 (Hlavacek-Larrondo et al. 2012), 3C 320 (Vagshette et al. 2019), 3C 444 (Vagshette et al. 2017), and 3C 220.1 (this work). Large solid square represents the cavity power of 3C 220.1 estimated from X-ray cavities, and empty square represents the power estimated based on the radio lobes (both not corrected for projection). For comparison, we show FR-II sources with jet power estimated from other methods, i.e., based on the properties of hotspots (blue plus; Godfrey & Shabala 2013), and from FR-II lobes with X-ray IC emission detections (magenta star; Ineson et al. 2017). See details in Section 4.2.

the upper limit for the angle of cavity to the line of sight. We found that the estimated cavity power of 3C 220.1 increases with decreasing angle of the cavity to the line of sight, e.g., the cavity power is $\sim 20\%$ larger for an angle of 60 degrees and $\sim 80\%$ larger for 30 degrees.

For comparison, we estimated the jet power using other techniques. The jet power can be estimated from the observed parameters of the jet terminal hotspots as $Q_{hs} = Ac\frac{B_{eq}^2}{8\pi} \times g_{hs}$ (e.g., Godfrey & Shabala 2013), where A is the area of the jet hotspots, c is the speed of light, B_{eq} is the equipartition magnetic field strength, and g_{hs} is the normalization factor, which can be empirically determined. Based on the 5 GHz radio flux at the eastern and western hotspots (Hardcastle et al. 2004), we estimate an equipartition magnetic field of ~ 100 μG for each hotspot (e.g., Miley 1980). From three hotspots, each with a radius of ~ 1.8 kpc, and a g_{hs} factor of 2, we estimate a total jet power of $\sim 6.9 \times 10^{45}$ erg s^{-1}. The properties of hotspots are thought to be variable on timescales comparable to the light crossing time of a hotspot, and the jet power estimated from this technique could vary on a timescale much shorter than that used to estimate the cavity power. We note that jet power is about four times the estimated cavity power based on the radio lobes.

For a sample of powerful FR-II radio galaxies with X-ray inverse Compton (IC) emission detections, Ineson et al. (2017) show that their radio lobes are typically dominated by relativistic electrons, and are in pressure balance at lobe mid-point but over-pressured in their outer parts relative to the external medium (e.g., Croston et al. 2017). They presented another method to estimate the time-averaged jet power as $Q_{jet} \sim 2E_i/t \sim 2E_i \times v/l$, where E_i is the internal energy of the lobe, t is the age of the jet, l is the lobe length, and v is the advance speed of the lobe, estimated directly from lobe overpressuring. With the enhanced X-ray emission possibly arising from IC emission (see Section 4.6), we estimated the internal pressure of 3C 220.1 and then its jet power. We used the `SYNCH`[4] code (Hardcastle et al. 1998) and assumed a power law in electron energy with Lorentz factors between $\gamma_{min} = 10$ and $\gamma_{max} = 10^5$ with an energy index of 2.4. The eastern and western radio lobes are approximated as spheres with radii of ~ 34 kpc and ~ 35 kpc respectively, and their radio flux densities are from Croston et al. (2005). We found that the observed magnetic field strengths of the eastern and western lobes are $\sim 0.46B_{eq}$ and $\sim 0.38B_{eq}$, respectively, close to the median value, $0.4B_{eq}$, found in Ineson et al. (2017). We obtain internal pressures of $\sim 5.0 \times 10^{-12}$ Pa and $\sim 7.0 \times 10^{-12}$ Pa for the eastern and western lobes, respectively, and the ratio to the external ICM pressures at the lobe mid-point are ~ 0.4 and ~ 0.8. Therefore, based on the internal pressure, the pressure difference at the lobe-tip, and the gas temperature (see Table 1), we estimate a jet power of $\sim 1.7 \times 10^{45}$ erg s^{-1}, which is consistent with the estimated cavity power based on the sizes of radio lobes. We notice that the radio lobes appear slightly under-pressured with respect to the environment, and 3C 220.1 seems not follow the relation between the internal and external pressure presented in Croston et al. (2017), especially for the eastern lobe. However, the Croston et al. (2017) relation is obtained from the studies of FR-II radio galaxies in galaxy groups. It has not been tested for the FR-IIs in massive galaxy clusters, where the pressure is much higher. In addition, since 3C 220.1 resides in a denser environment, where the lobes are in direct contact with the ICM, any entrained non-radiating particles will increase the internal pressure of the lobes. Alternatively, the lobe pressure may be dominated by the kinetic and thermal energy of shocked gas, as for example in PKS B2152-699 (Worrall et al. 2012). Therefore, the jet power of 3C 220.1 could be under-estimated.

In Fig. 9 we plot the radio power versus cavity power for FR-I sources and FR-II radio sources available from the literature (Bîrzan et al. 2008; Cavagnolo et al. 2010; O'Sullivan et al. 2011; Worrall et al. 2012; Vagshette et al. 2017; Liu et al. 2019; Hlavacek-Larrondo et al. 2012). For comparison, we also show FR-II sources with their jet power estimated from two other techniques discussed above (Godfrey & Shabala 2013; Ineson et al. 2017). We converted their radio luminosities at 151 MHz to the corresponding ones at 1.4 GHz assuming a spectral index of 0.7. There are six common systems in two studies but the quoted radio luminosities and jet power are generally different, with the radio luminosity ratios from $0.2 - 2.8$ (a median value of 0.6) and the jet power ratios from $0.8 - 9.6$ (a median value of 3.8). As shown in Fig. 9, the jet power estimated from two different methods are generally consistent for very luminous radio galaxies (e.g., $P_{1400} >\sim 3 \times 10^{26}$ W Hz^{-1}). However, the power estimated from X-ray cavities are systematically smaller than the jet power estimated from those two methods, especially for the

[4] https://github.com/mhardcastle/pysynch

cavity power of 3C 220.1 determined from the inner pair of X-ray cavities. We suggest the cavity power of 3C 220.1, or similar FR-II source, is under-estimated due to one or more of the following reasons: 1) A large amount of energy from the central SMBH is released as radiation power of the central AGN; 2) Much of the energy of the central SMBH could be deposited in a shock, which either has dissipated, or is hard to detect in high redshift systems; 3) The sizes of cavities are under-estimated due to the complex structures, e.g., the bright central AGN and the enhancements in the lobes, projection and the limited data statistics.

We note that Fig. 9 contains both FR-I and FR-II radio galaxies and the two populations may not be fully comparable due to their different intrinsic properties and environment. To maintain pressure balance with the external medium, their lobe internal composition is thought to be different, with FR-I lobes containing more protons (e.g., Croston et al. 2018). Therefore, the jet powers of the two populations are expected to be systematically different due to a high fraction of non-radiating particles present in FR-I galaxies. In addition, the radio luminosity of an AGN depends on the jet power and external pressure (e.g., Hardcastle & Krause 2013) so a radio galaxy embedded in higher pressure environment would require a lower jet power to produce the same radio luminosity.

4.3 Radiative and Kinetic Power

Fig. 10 shows the comparison of the AGN nuclear 2-10 keV luminosity with the cooling luminosity, the cavity power, and the radio power for BCGs. Fig. 11 shows the cavity enthalpy versus the 2-10 keV nuclear luminosity. We included the samples from Hlavacek-Larrondo & Fabian (2011) and Hlavacek-Larrondo et al. (2013), and three quasar systems, the Phoenix cluster (McDonald et al. 2012, 2015), H1821+643 (Russell et al. 2010) and IRAS 09104+4109 (Vignali et al. 2011; O'Sullivan et al. 2012). The nuclear luminosities in the plot span more than five orders of magnitude. The properties of 3C 220.1 are similar to those of quasars. Both "quasars" and "radio galaxies" have luminous central AGNs, and energetic jets which extend outwards, inflate radio lobes, and create X-ray cavities. The nuclear luminosity of 3C 220.1 is the third largest in the plot, and is much greater than both the cooling luminosity and the cavity power. The ratio of nuclear luminosity (in the 2-10 keV band) to the cavity power for 3C 220.1 is ~ 5, which is the second largest and only smaller than the ratio for H1821+643 (~ 28). Weak cavities could be missed and the cavity power in the middle panel can be taken as a lower limit. If we assume that the cavities in 3C 220.1 have the same size as the radio lobes, the cavity power would be almost 20 times larger, as shown by the open circle in the middle panel of Fig. 10. As an FR-II radio galaxy, 3C 220.1 produces a larger radio power than the three quasars shown.

A SMBH and its surrounding medium are expected to evolve through two stages (e.g., see Fabian 2012, and references therein). According to a standard paradigm, at early times the SMBH grows rapidly by accreting cooling gas at high rate, and AGN feedback is radiation dominated in the so-called "quasar-mode" (e.g., Springel et al. 2005; Hopkins et al. 2006; Sijacki & Springel 2006). The SMBH produces enough power to suppress cooling, quenching star formation, and regulating the growth of the SMBH. As the SMBH is starved of fuel and the accretion rate drops, the system evolves to the "radio-mode", where mechanical dominated feedback regulates radiative cooling in the ICM in the form of bubbles and shocks (e.g., McNamara & Nulsen 2007; Fabian 2012). With a high accretion rate ($\sim$10% of the Eddington rate), 3C 220.1 is currently in quasar-mode. However, there is also evidence of mechanical heating, e.g., the radio jet and the X-ray cavities, and the mechanical power is able to compensate for the cooling losses of the ICM. Therefore, 3C 220.1 may be at the transition stage in which the SMBH has not evolved completely out of quasar-mode, but already produces sufficient power to suppress cooling.

Unlike most of the powerful FR-II galaxies at high redshift, 3C 220.1 lives in a dense environment. AGN activity with a high accretion rate can be triggered by a recent galaxy merger or interaction (e.g., Ramos Almeida et al. 2011; Pierce et al. 2019), as shown by the distorted morphology in *HST* image (Fig. 2) and the high star formation rate (section 4.4). We can estimate the time elapsed since the last interaction and how long the AGN has been accreting in its current mode through the spectral age. Assuming the magnetic field is constant and the particle injected have a constant power-law energy spectrum, the spectral age is given by (e.g., Jamrozy et al. 2008):

$$t = 50.3[\nu(1+z)]^{-1/2}\frac{B^{1/2}}{B^2+B_{ic}^2}\mathrm{Myr}, \quad (2)$$

where $B_{ic} = 0.32(1+z)^2$, is the magnetic field strength in units of nT equivalent to the cosmic microwave background radiation, B is the magnetic field strength of the radio lobes in nT, ν is the spectral break frequency in GHz. Although there is too little radio data to measure spectral curvature with sufficient angular resolution, the steep spectrum in lobe suggests that the spectral break is below about 5 GHz. Using an equipartition magnetic field of $\sim$ 3 nT, we estimate a lower limit to the age of $\sim$ 3.2 Myr.

4.4 BCG and Star Formation

3C 220.1 has a 24 μm flux density of 2.2$\pm$0.2 mJy measured from *Spitzer* (Cleary et al. 2007) and remains undetected at 70 μm, 100 μm and 160 μm from *Spitzer* and *Herschel*. We assume an average spectral index of -0.3 between the rest-frame 15 μm and 30 μm from the same work. The SFR of the BCG is then estimated to be about 60 - 80 $M_\odot$/yr from the calibrations of Lee et al. (2013) and Rieke et al. (2009), assuming a Kroupa IMF. This is consistent with the estimate from Westhues et al. (2016) and comparable to the SFR of another high redshift cluster IRAS 09104+4109 ($z = 0.44$) also with a luminous central AGN (O'Sullivan et al. 2012). Substantial SF in the BCG of 3C 220.1 is also implied by its distorted morphology as seen with *HST* (Fig. 2). However, this estimate of SFR may be biased high if there is still a significant contribution from the AGN in the observed 24 μm band.

4.5 Deflected Radio Jet

Fig. 1 (bottom right) shows a deflected radio jet (with an angle of $\sim 14^\circ$) on the eastern side in the VLA 8.4 GHz

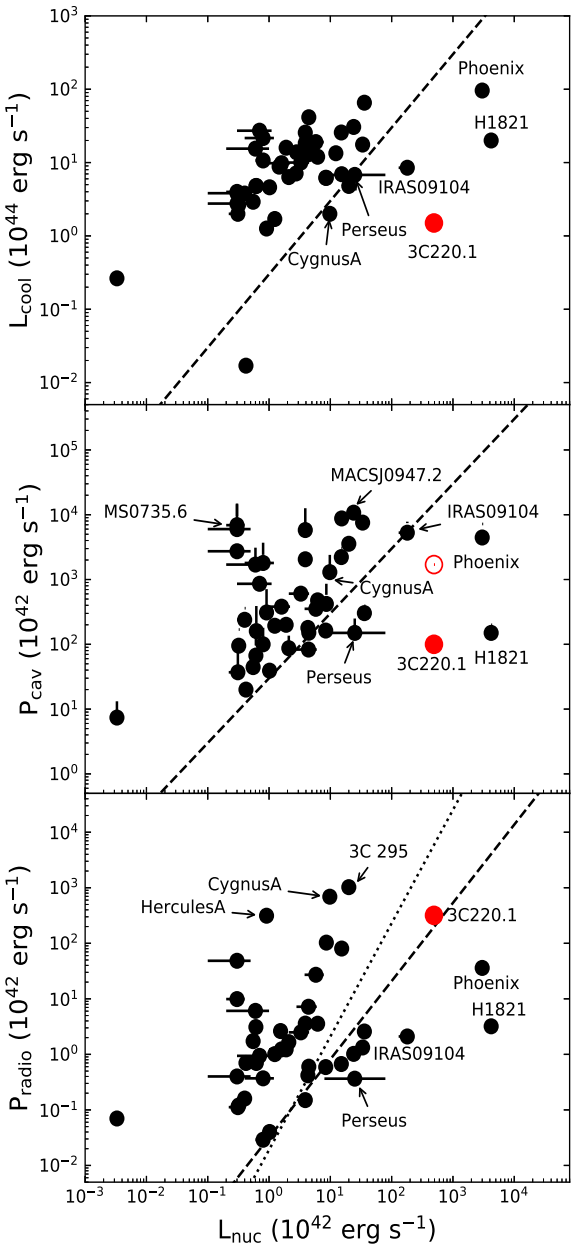

Figure 10. Top: The bolometric cooling luminosity versus nuclear 2-10 keV luminosity. The black dotted line represents equal cooling and bolometric luminosity of central AGN, assuming a bolometric correction factor of 30. Middle: Cavity power versus nuclear 2-10 keV luminosity. The dashed line is the equal line of cavity power and bolometric luminosity. Bottom: Total radio power (10 MHz to 10 GHz) versus nuclear 2-10 keV luminosity. The dashed and dotted lines are the equal lines of the nuclear bolometric luminosity and the cavity power, which are calculated based on the relation between the radio power and cavity power from Bîrzan et al. (2008) and O'Sullivan et al. (2011), respectively. The red circles are for 3C 220.1. The empty red circle in the middle panel represents 3C 220.1, assuming that the cavities have the same size as the radio lobes. H1821+643 data are from Russell et al. (2010). Phoenix Cluster data are from McDonald et al. (2012) and McDonald et al. (2015). IRAS 09104+4109 data are from Vignali et al. (2011) and O'Sullivan et al. (2012). Data of other black circles are from Hlavacek-Larrondo & Fabian (2011) and Hlavacek-Larrondo et al. (2013). Note that all the AGNs are located in the cluster BCGs.

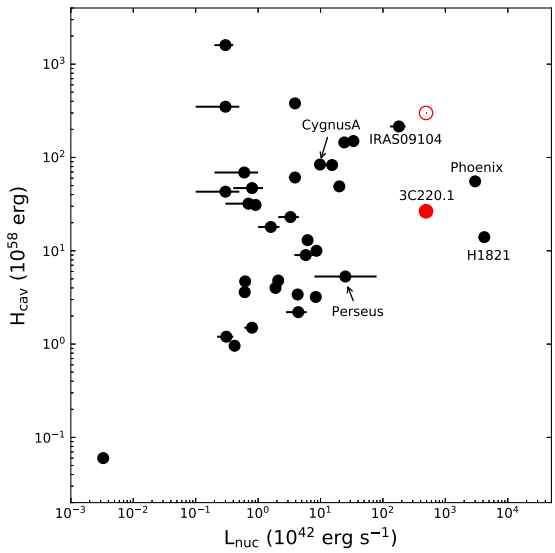

Figure 11. Similar to Fig. 10, but for cavity enthalpy ($H_{\rm cav} = 4PV$) versus nuclear 2-10 keV luminosity. The empty red circle represents 3C 220.1 assuming that the cavities have the same size of the radio lobes.

map. It is almost straight to the bending point ($\sim 6''$ from the nucleus), and almost straight from that point to the second eastern hotspot (e.g., Mullin et al. 2006), which may be where the jet partially de-collimates before being turned around the edge of the lobe into the first hotspot. This cannot be explained with the dentist's drill model (Scheuer 1974). In the dentist's drill model, when a hotspot is no longer being fed directly by the jet it will stop advancing and will expand to merge into the general radio lobe. This should happen rather fast, since the hotspot is a locus of high pressure excess, and the expansion time (greater than the radio fading time) is expected to be short compared with the jet propagation time from the core to the edge of the lobe.

As described in Mullin et al. (2006), the flow continues from the jet to hotspots, and bends around to the south and back toward the core. The jet deflection point lies close to the edge (in projection) of the low-frequency radio lobe, so a natural explanation would be that the jet flow is encountering some angled interface between two different environments - passing into plasma dominated by the radio lobe. The structure can be interpreted in terms of low-density supersonic fluid flows with interactions causing the jets to change direction by a small angle until they slow down or encounter strong shocks.

In Krause et al. (2019), the radio features of 3C 220.1 in the VLA 8.4 GHz image, such as jet curvature, jet at the edge of lobe, and the wide terminal hotspots on both sides, are considered as a result of jet precession. Jet precession usually produces curving jets, with S-symmetry if both jet and counter-jet are observed. Simple jet precession would have problems producing two such straight segments with a single bend. However, depending on the viewing angle, the jet can appear with mild curvature or as a straight jet.

4.6 Enhanced X-ray Emission in the Radio Lobes

Powerful FR II radio sources show extended lobes of synchrotron-emitting plasma, as well as the jets which terminate in bright hotspots. The radio plasma displaces the hot ICM, forming X-ray cavities, and compresses it into a dense shell, which may be observed as a sharp bright edge in X-rays and is referred as the cocoon shock. One of the best-studied examples is the nearest powerful FR II source, Cygnus A (e.g., Wilson et al. 2006; Snios et al. 2018). As a powerful FR II source at a higher redshift, 3C 220.1 shows structure similar to Cygnus A. In Fig. 12 we show the *Chandra* images of 3C 220.1 and Cygnus A side by side. Assuming that Cygnus A is observed at a similar redshift to 3C 220.1's, we re-binned the X-ray flux image of Cygnus A by a factor of 6 based on the pixel scale ratio at the two different redshifts (the actual pixel scale ratio is 6.19), then re-scaled it by the ratio of squared luminosity distances. The final image is then rotated to have similar tilted radio structures as 3C 220.1. Interesting features of the two systems are within similar physical scales ($\sim$ 100 kpc, the red circles in Fig. 12). Along the radio jet direction away from the central bright region, both systems show X-ray cavities in the radio lobes, and enhanced X-ray emission in the region toward the hotspots. Outside the radio lobes, there is a possible shock edge in 3C 220.1, which is difficult to confirm through the surface brightness profile due to the limited counts.

X-ray emission in the lobes can have contributions from inverse Compton (IC) emission, produced by photons being IC-scattered to X-ray energies by the radio-synchrotron emitting electrons. IC emission has been observed in many FR II radio lobes (e.g., Isobe et al. 2002; Bondi et al. 2004; Hardcastle & Croston 2010; Croston et al. 2005; Ineson et al. 2017; de Vries et al. 2018). In order to check for IC X-ray emission in the lobes, we chose two elliptical regions for the lobes based on Fig. 4, and two off-lobe regions for each lobe, as shown in Fig. 13. We extracted the spectra from those regions from each observation. The spectra from the two off-lobe regions are combined with the ciao tool `combine_spectra`. The spectra from the lobe regions show clear excesses over those from off-lobe regions. Assuming the thermal emission from the hot ICM is the same in lobe- and off-lobe regions, we found that an extra power-law component with fixed index of 2.0 helps to fit the excess, suggesting the enhanced X-ray emission is of non-thermal origin. We obtained values for the power-law normalization at 1 keV of 0.5 nJy and 0.8 nJy for the eastern and western lobes, respectively, and luminosities at 2-10 keV of $\sim 3 \times 10^{42}$ and $\sim 5 \times 10^{42}$ erg s^{-1}. Considering the lobe regions in our study are smaller than those in Croston et al. (2005), our estimates are consistent with their results. However, we found a second thermal component with a high temperature (e.g., $\sim$ 6 keV) can also fit the excess. Due to the limited data statistics, we cannot make a definitive conclusion as to which model better describes the enhanced emission.

5 SUMMARY

3C 220.1 is an FR-II radio galaxy which is undergoing strong radiative feedback. We have analyzed 174 ks of *Chandra* observations centered on the BCG of this $kT \sim 4$ keV galaxy cluster and presented the properties of the hot gas related to AGN feedback. Our results are summarized as follows:

- The X-ray emission of the central AGN dominates the central $\sim 2''$. The bolometric luminosity is estimated to be 2.0×10^{46} erg s^{-1}, among the highest known for a cluster BCG. Assuming a radiative efficiency of 0.1, we estimate an Eddington ratio of ~ 0.13.
- We found a pair of potential X-ray cavities to the eastern and western sides of the AGN based on the surface brightness depressions. The total enthalpy and cavity power for the cavities are estimated to be 2.7×10^{59} erg and $\sim 1.0 \times 10^{44}$ erg s^{-1}. This cavity power is comparable to the cooling luminosity of the cluster. If the X-ray cavities are assumed to be as large as the radio lobes, the total enthalpy and cavity power become ~ 11 and ~ 17 times larger. Furthermore, if we consider the effect of projection, the cavity power could be double our estimate if the lobes lie close to the line of sight. Using two other techniques we estimated the jet power of 6.9×10^{45} erg s^{-1} and 1.7×10^{45} erg s^{-1} for 3C 220.1 based on the hotspot properties and the properties of lobes with X-ray IC emission detections, respectively. The cavity power of 3C 220.1 and other FR-II sources, being systematically smaller than the jet power estimated from those two methods, could be well under-estimated.
- A likely explanation of the X-ray enhancements in the radio lobes of 3C 220.1 is IC emission. We estimate 2-10 keV luminosities of $\sim 3 \times 10^{42}$ and $\sim 5 \times 10^{42}$ erg s^{-1} from the eastern and western lobes, respectively.
- The properties of 3C 220.1 are similar to those of quasars. The ratio of X-ray nuclear luminosity to cavity power is $\sim$ 5, which is the second largest known among BCGs after the source H1821+643. We suggest that 3C 220.1 is at the transition stage from quasar-mode feedback to radio-mode feedback.

6 ACKNOWLEDGEMENTS

We thank the referee for important comments and suggestions. Support for this work was provided by the National Aeronautics and Space Administration through *Chandra* Award Number GO5-16115X, GO7-18118X and AR7-18016X issued by the *Chandra* X-ray Center, which is operated by the Smithsonian Astrophysical Observatory for and on behalf of the National Aeronautics Space Administration under contract NAS8-03060. We also acknowledge the support from NASA/EPSCoR grant NNX15AK29A and NSF grant 1714764. This research has made use of data and/or software provided by the High Energy Astrophysics Science Archive Research Center (HEASARC), which is a service of the Astrophysics Science Division at NASA/GSFC and the High Energy Astrophysics Division of the Smithsonian Astrophysical Observatory. The NRAO *VLA* Archive Survey image was produced as part of the NRAO *VLA* Archive Survey, (c) AUI/NRAO.

REFERENCES

Asplund M., Grevesse N., Sauval A. J., Scott P., 2009, ARA&A, 47, 481

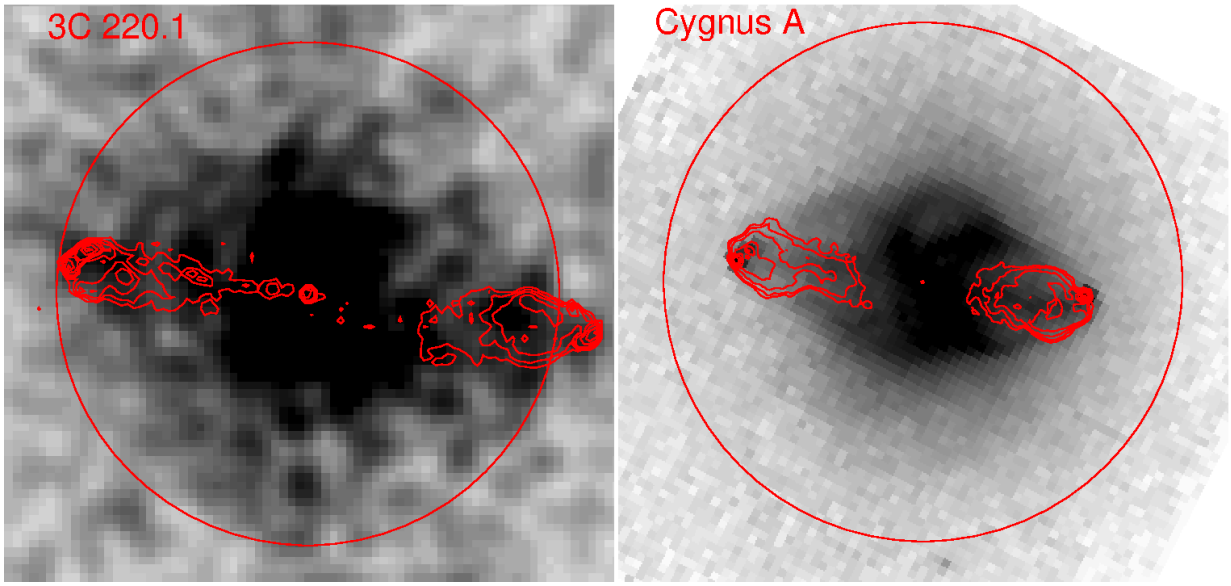

Figure 12. Comparison of *Chandra* background-subtracted, exposure-corrected images of 3C 220.1 (left) overlaid with VLA 8.4 GHz contours and Cygnus A (right) overlaid with VLA 1.5 GHz contours. The Cygnus A image has been rotated to the same orientation as 3C 220.1, with the side with a one-sided jet at small radii on the left as in 3C 220.1. The radii of the red circles are 100 kpc. To roughly simulate the X-ray image of Cygnus A at 3C 220.1's redshift, the X-ray image of Cygnus A has been re-binned by a factor of 6, and then re-scaled by the ratio of the squared luminosity distances.

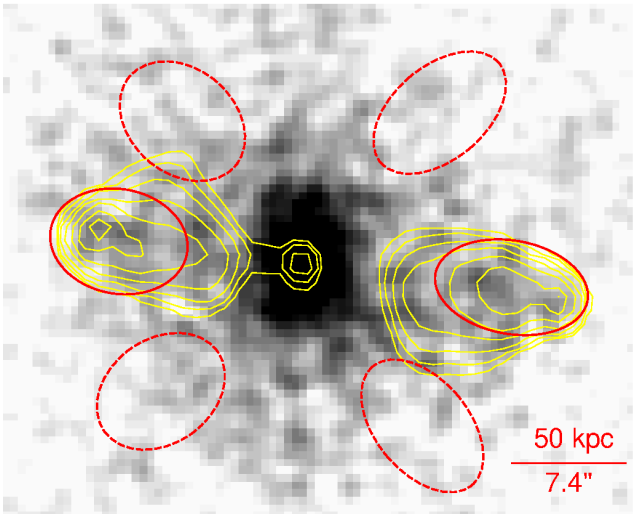

Figure 13. Regions used to study the diffuse X-ray emission in the lobes of 3C 220.1. The radio contours at VLA 1.5 GHz are shown in yellow. Solid ellipses are regions used for the eastern and western lobes; Dashed ellipses indicate the off-lobe regions.

Belsole E., Worrall D. M., Hardcastle M. J., 2006, MNRAS, 366, 339
Belsole E., Worrall D. M., Hardcastle M. J., Croston J. H., 2007, MNRAS, 381, 1109
Bîrzan L., McNamara B. R., Nulsen P. E. J., Carilli C. L., Wise M. W., 2008, ApJ, 686, 859
Bondi M., Brunetti G., Comastri A., Setti G., 2004, MNRAS, 354, L43
Carter C., Karovska M., Jerius D., Glotfelty K., Beikman S., 2003, in Payne H. E., Jedrzejewski R. I., Hook R. N., eds, Astronomical Society of the Pacific Conference Series Vol. 295, Astronomical Data Analysis Software and Systems XII. p. 477
Cash W., 1979, ApJ, 228, 939
Cavagnolo K. W., McNamara B. R., Nulsen P. E. J., Carilli C. L., Jones C., Bîrzan L., 2010, ApJ, 720, 1066
Churazov E., Brüggen M., Kaiser C. R., Böhringer H., Forman W., 2001, ApJ, 554, 261
Cleary K., Lawrence C. R., Marshall J. A., Hao L., Meier D., 2007, ApJ, 660, 117
Comerford J. M., Natarajan P., 2007, MNRAS, 379, 190
Croston J. H., Hardcastle M. J., Harris D. E., Belsole E., Birkinshaw M., Worrall D. M., 2005, ApJ, 626, 733
Croston J. H., Hardcastle M. J., Mingo B., Evans D. A., Dicken D., Morganti R., Tadhunter C. N., 2011, ApJ, 734, L28
Croston J. H., Ineson J., Hardcastle M. J., Mingo B., 2017, MNRAS, 470, 1943
Croston J. H., Ineson J., Hardcastle M. J., 2018, MNRAS, 476, 1614
Davis J. E., 2001, ApJ, 562, 575
Dunn R. J. H., Fabian A. C., 2006, MNRAS, 373, 959
Fabian A. C., 2012, ARA&A, 50, 455
Fernini I., 2014, ApJS, 212, 19
Gaspari M., Ruszkowski M., Sharma P., 2012, ApJ, 746, 94
Giles P. A., et al., 2016, A&A, 592, A3
Giovannini G., Feretti L., Gregorini L., Parma P., 1988, A&A, 199, 73
Godfrey L. E. H., Shabala S. S., 2013, ApJ, 767, 12
Gültekin K., Cackett E. M., Miller J. M., Di Matteo T., Markoff S., Richstone D. O., 2009, ApJ, 706, 404
Hardcastle M. J., Croston J. H., 2010, MNRAS, 404, 2018
Hardcastle M. J., Krause M. G. H., 2013, MNRAS, 430, 174
Hardcastle M. J., Lawrence C. R., Worrall D. M., 1998, ApJ, 504, 743
Hardcastle M. J., Harris D. E., Worrall D. M., Birkinshaw M., 2004, ApJ, 612, 729
Hlavacek-Larrondo J., Fabian A. C., 2011, MNRAS, 413, 313
Hlavacek-Larrondo J., Fabian A. C., Edge A. C., Ebeling H., Sanders J. S., Hogan M. T., Taylor G. B., 2012, MNRAS, 421, 1360
Hlavacek-Larrondo J., Fabian A. C., Edge A. C., Ebeling H., Allen

S. W., Sanders J. S., Taylor G. B., 2013, MNRAS, 431, 1638
Hlavacek-Larrondo J., et al., 2015, ApJ, 805, 35
Hopkins P. F., Hernquist L., Cox T. J., Di Matteo T., Robertson B., Springel V., 2006, ApJS, 163, 1
Humphrey P. J., Liu W., Buote D. A., 2009, ApJ, 693, 822
Ineson J., Croston J. H., Hardcastle M. J., Mingo B., 2017, MNRAS, 467, 1586
Isobe N., Tashiro M., Makishima K., Iyomoto N., Suzuki M., Murakami M. M., Mori M., Abe K., 2002, ApJ, 580, L111
Jamrozy M., Konar C., Machalski J., Saikia D. J., 2008, MNRAS, 385, 1286
Kaastra J. S., 2017, A&A, 605, A51
Krause M. G. H., et al., 2019, MNRAS, 482, 240
Lee J. C., Hwang H. S., Ko J., 2013, ApJ, 774, 62
Li J., Kastner J. H., Prigozhin G. Y., Schulz N. S., Feigelson E. D., Getman K. V., 2004, ApJ, 610, 1204
Liu W., et al., 2019, MNRAS, 484, 3376
Massaro F., et al., 2015, ApJS, 220, 5
McDonald M., et al., 2012, Nature, 488, 349
McDonald M., et al., 2015, ApJ, 811, 111
McNamara B. R., Nulsen P. E. J., 2007, ARA&A, 45, 117
Miley G., 1980, ARA&A, 18, 165
Mullin L. M., Hardcastle M. J., Riley J. M., 2006, MNRAS, 372, 113
O'Sullivan E., Giacintucci S., David L. P., Gitti M., Vrtilek J. M., Raychaudhury S., Ponman T. J., 2011, ApJ, 735, 11
O'Sullivan E., et al., 2012, MNRAS, 424, 2971
Pierce J. C. S., Tadhunter C. N., Ramos Almeida C., Bessiere P. S., Rose M., 2019, MNRAS, 487, 5490
Rafferty D. A., McNamara B. R., Nulsen P. E. J., Wise M. W., 2006, ApJ, 652, 216
Ramos Almeida C., Tadhunter C. N., Inskip K. J., Morganti R., Holt J., Dicken D., 2011, MNRAS, 410, 1550
Rieke G. H., Alonso-Herrero A., Weiner B. J., Pérez-González P. G., Blaylock M., Donley J. L., Marcillac D., 2009, ApJ, 692, 556
Russell H. R., Fabian A. C., Sanders J. S., Johnstone R. M., Blundell K. M., Brandt W. N., Crawford C. S., 2010, MNRAS, 402, 1561
Scheuer P. A. G., 1974, MNRAS, 166, 513
Sharma P., McCourt M., Quataert E., Parrish I. J., 2012, MNRAS, 420, 3174
Sijacki D., Springel V., 2006, MNRAS, 366, 397
Snios B., et al., 2018, ApJ, 855, 71
Spinrad H., Djorgovski S., Marr J., Aguilar L., 1985, PASP, 97, 932
Springel V., Di Matteo T., Hernquist L., 2005, MNRAS, 361, 776
Sun M., 2012, New Journal of Physics, 14, 045004
Sun M., Forman W., Vikhlinin A., Hornstrup A., Jones C., Murray S. S., 2003, ApJ, 598, 250
Sun M., Voit G. M., Donahue M., Jones C., Forman W., Vikhlinin A., 2009, ApJ, 693, 1142
Vagshette N. D., Naik S., Patil M. K., Sonkamble S. S., 2017, MNRAS, 466, 2054
Vagshette N. D., Naik S., Patil M. K., 2019, arXiv e-prints,
Vasudevan R. V., Fabian A. C., 2007, MNRAS, 381, 1235
Vignali C., et al., 2011, MNRAS, 416, 2068
Voit G. M., 2005, Reviews of Modern Physics, 77, 207
Voit G. M., Bryan G. L., O'Shea B. W., Donahue M., 2015, ApJ, 808, L30
Westhues C., et al., 2016, AJ, 151, 120
Wilson A. S., Smith D. A., Young A. J., 2006, ApJ, 644, L9
Worrall D. M., Birkinshaw M., 2017, MNRAS, 467, 2903
Worrall D. M., Birkinshaw M., Hardcastle M. J., Lawrence C. R., 2001, MNRAS, 326, 1127
Worrall D. M., Birkinshaw M., Young A. J., Momtahan K., Fosbury R. A. E., Morganti R., Tadhunter C. N., Verdoes Kleijn G., 2012, MNRAS, 424, 1346
de Vries M. N., et al., 2018, MNRAS, 478, 4010